Title
Accuracy and noise in optical Doppler tomography studied by Monte Carlo simulation.

Journal
Physics in medicine and biology, 43(10)

ISSN
0031-9155

Authors
Lindmo, T
Smithies, DJ
Chen, Z
et al.

Publication Date
1998-10-01

DOI
10.1088/0031-9155/43/10/025

Phys. Med. Biol. **43** (1998) 3045–3064. Printed in the UK PII: S0031-9155(98)91632-3

Accuracy and noise in optical Doppler tomography studied by Monte Carlo simulation

Tore Lindmo†‡, Derek J Smithies‡, Zhongping Chen‡, J Stuart Nelson‡ and Thomas E Milner‡

† Department of Physics, Norwegian University of Science and Technology, N-7034 Trondheim, Norway

‡ Beckman Laser Institute and Medical Clinic, University of California at Irvine, Irvine, CA 92612, USA

Received 6 February 1998

Abstract. A Monte Carlo model has been developed for optical Doppler tomography (ODT) within the framework of a model for optical coherence tomography (OCT). A phantom situation represented by blood flowing in a horizontal 100 μm diameter vessel placed at 250 μm axial depth in 2% intralipid solution was implemented for the Monte Carlo simulation, and a similar configuration used for experimental ODT measurements in the laboratory.

Simulated depth profiles through the centre of the vessel of average Doppler frequency demonstrated an accuracy of 3–4% deviation in frequency values and position localization of flow borders, compared with true values.

Stochastic Doppler frequency noise was experimentally observed as a shadowing in regions underneath the vessel and also seen in simulated Doppler frequency depth profiles. By Monte Carlo simulation, this Doppler noise was shown to represent a nearly constant level over an investigated 100 μm interval of depth underneath the vessel. The noise level was essentially independent of the numerical aperture of the detector and angle between the flow velocity and the direction of observation, as long as this angle was larger than 60°. Since this angle determines the magnitude of the Doppler frequency for backscattering from the flow region, this means that the signal-to-noise ratio between Doppler signal from the flow region to Doppler noise from regions underneath the flow is improved by decreasing the angle between the flow direction and direction of observation. Doppler noise values from Monte Carlo simulations were compared with values from statistical analysis.

1. Introduction

Optical Doppler tomography (ODT) (Wang *et al* 1995a) combines the technique of optical coherence tomography (OCT) with detection of the Doppler shift of backscattered light. ODT permits determination of localized flow velocities in optically turbid media and can be used to image blood flow in biological tissues. Experimental investigations have demonstrated good results for ODT, both for *in vitro* experimental flow configurations and for imaging of *in vivo* blood flow (Chen *et al* 1997a, b, c, Wang *et al* 1995a, b, 1997). The parabolic flow profile predicted from hydrodynamic theory for laminar flow in cylindrical tubes has been precisely demonstrated in experimental systems and shown to give the correct mean flow velocity (Wang *et al* 1995a). Blood is, however, a strongly scattering medium, and multiple scattering effects are expected to occur in all but the most tiny blood capillaries, since the scattering mean free path in blood is only about 7 μm.

0031-9155/98/103045+20$19.50

For uniform velocity fields (i.e. constant unidirectional velocity, independent of r) it can be easily shown that the resulting Doppler shift from multiple scattering events in the flowing medium is determined only by the scalar product between the velocity vector and the difference between the outgoing and incoming wavevectors (de Mul *et al* 1995). For fixed incoming and outgoing beam directions, the accumulated Doppler shift reported by the outgoing photon will therefore be independent of the number and locations of intermediate scattering events.

However, it is not difficult to construct examples for the more realistic and interesting case of a variable, for example parabolic velocity distribution, where the total Doppler shift reported by a photon that undergoes two scattering events will be very different from the exact value reported from a single backscattering event. Furthermore, the apparent backscatter position that will be ascribed to the detected photon will be different from the position of either one of the two scattering events. Such thought experiments raise the question whether experimental ODT yields such good results because the technique is sufficiently selective in photon detection that it essentially represents measurements based on singly (back)scattered photons. Alternatively, the technique of averaging the Doppler shift for many photons detected from the position under investigation may be sufficiently robust to yield correct results even in the presence of significant multiple scattering effects.

Monte Carlo simulation has already been used successfully in studies of laser Doppler flowmetry (LDF) (de Mul *et al* 1995, Jentink *et al* 1990, Koelnik *et al* 1994, Stern 1993). LDF is different from ODT in that LDF utilizes a highly coherent source and therefore the technique gives no pathlength discrimination. However, the fundamental Monte Carlo modelling which simulates light propagation in the medium and Doppler shifts experienced at each interaction with a moving scatterer is the same for the two techniques.

We have included in the model pathlength gating defined by the coherence length of the light source, and a geometrical optics representation of the combined emission and detection probe used in ODT, as described in more detail in a companion paper (Smithies *et al* 1998). With this model we can study how instrumentation parameters and properties of the flowing medium and its surroundings might influence the numerical and positional accuracy of velocities determined by ODT. A simple flow geometry was used in which a parabolic velocity profile was established in a vessel at a specified depth in a scattering medium, and a physical phantom representing the same features was used for laboratory experiments.

2. Materials and methods

2.1. Experimental ODT system

2.1.1. Instrumentation. The ODT instrument uses a fibre-optic Michelson interferometer with a low-coherence superluminescent diode (SLD) as the light source. Details of this instrument have been described previously (Chen *et al* 1997a, b, Wang *et al* 1997) and in the companion paper (Smithies *et al* 1998).

The optical phase of the SLD light in both the probe and reference arms of the interferometer is modulated at 1600 Hz by stretching the optical fibre wrapped around piezoelectric cylinders driven by a ramp waveform. Optical interference fringe intensity is measured by a silicon photovoltaic receiver (New Focus 2001, New Focus Inc., Santa Clara, CA). The signal is digitized with a 16-bit analogue–digital converter and transferred to a computer workstation for processing. The interference fringe intensity at each pixel is transformed by a fast Fourier transform algorithm. A power spectrum of interference fringe

intensity for the position (x, z') as a function of frequency f is calculated as

$$G_f(x, z_i', f) = |\mathrm{STFFT}(f, G_t(x, z_i', t))|^2. \tag{1}$$

STFFT is the short-time fast Fourier transform of the temporal interference fringe intensity $G_t(x, z_i', t)$, and the primed z' indicates the focus depth in the medium after refraction at the surface. A tomographic structural image is obtained by calculating the relative reflectivity which equals the value of the power spectrum at the phase modulation frequency (f_0). A logarithmic scale is used to display the ODT structural image:

$$S(x, z_i') = 10 \log_{10}(G_f(x, z_i', f_0)). \tag{2}$$

Fluid flow velocity at each pixel is calculated from the Doppler frequency shift $\Delta f_D = \Delta\omega_D/2\pi$ which is determined as the difference between the centroid (f_c) of the measured power spectrum and the carrier frequency established by the optical phase modulation (f_0):

$$v_{\mathrm{ODT}}(x, z_i') = \lambda(f_c - f_0)/2\cos\varepsilon. \tag{3}$$

Here we have assumed ideal backscattering ($\Delta\boldsymbol{k} = \boldsymbol{k}_o - \boldsymbol{k}_i = -2\boldsymbol{k}_i$), where $\boldsymbol{k}_i$ and $\boldsymbol{k}_o$ are the incoming and outgoing wavevectors respectively. $\lambda = 2\pi/k$ is the centre wavelength of the SLD source, and $\varepsilon = 90^\circ - \alpha$ is the angle between $\Delta\boldsymbol{k}$ and $\boldsymbol{v}$ in air. The centroid of the measured power spectrum at each pixel is given by

$$f_c = \sum_{j=1}^{m} f_j G_f(x, z_i', f_j) / \sum_{j=1}^{m} G_f(x, z_i', f_j) \tag{4}$$

where m is the number of frequency intervals used in the estimation of $G_f(x, z_i', f)$. Lateral and axial spatial resolutions of our ODT instrument are limited by the beam spot size and source coherence length (L_c) to 5 and 13 μm respectively. Velocity resolution in our prototype instrument (100 μm s^{-1}) depends on pixel acquisition time ΔT and the angle (ε) between flow velocity ($\boldsymbol{v}$) and the direction of observation ($\boldsymbol{k}_o$). Velocity resolution may be improved with a smaller angle ε or longer acquisition time.

2.1.2. Flow phantoms. Canine blood was chosen as a model system due to the expected similarity in optical properties with human blood. Human and canine erythrocytes (RBCs) have average diameters of 7.8 and 7.2 μm, and thicknesses of 2.06 and 1.95 μm respectively (Hawkey and Dennett 1989). Packed canine RBCs (Hemopet, Irvine, CA) were fixed with glutaraldehyde to yield a stock suspension of single cells that could be reconstituted at any desired volume ratio of cells (i.e. haematocrit). Prior to experimentation a stable, non-sedimenting model of blood was made by resuspending glutaraldehyde-fixed RBCs from stock at the specified volume fraction in 42% CsCl (Optical Grade, Sigma, St Louis, MO) which has a density of 1.31 and refractive index of 1.36 (Weast *et al* 1984). Inspection by microscopy confirmed that the suspension contained predominantly single cells of normal shape.

The geometry of our *in vitro* blood flow phantom is shown in figure 1A. A syringe pump (model 341A, Sage Instruments, Cambridge, MA) with a 500 μl Hamilton syringe (#1750, Hamilton, Reno, NV) was used to establish flow of the reconstituted blood through polyethylene tubing (P10, id 0.28 mm, od 0.61 mm, Clay Adams/Becton Dickinson, Sparks, MD) immersed in 1 or 2% intralipid (Intralipid 20%, Kabi Pharmacia Inc., Clayton, NC)

Since erythrocyte shape was well preserved after fixation, the optical parameters of the reconstituted canine blood were taken to be the same as for human blood. Optical parameters for blood at 850 nm were adopted from Jacques (1996) and Yaroslavsky *et al* (1996). Both authors give values of $\mu_a = 0.75$ mm^{-1}, but values for μ_s of 300 mm^{-1}

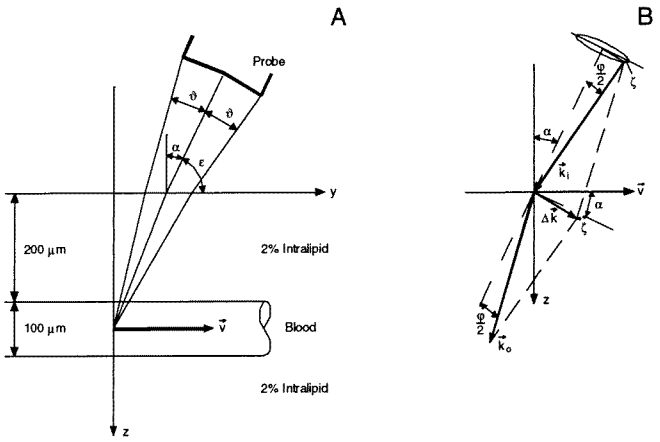

Figure 1. A: Geometry of ODT flow phantom for Monte Carlo simulations. A 100 μm diameter wall-less tube is positioned horizontally in a 2% intralipid solution at an axial depth of 250 μm. The y-axis is taken to be parallel to the tube axis. The probe is aimed with an incidence angle of α at various focus positions z' on the z-axis through the centre of the tube lumen. B: Vector diagram illustrating forward scattering according to equation (5). The angle α changes to α' in the medium.

and 65 mm^{-1} respectively, and g-values of 0.996 and 0.99 respectively. We chose to use $\mu_a = 0.75$ mm^{-1}, $\mu_s = 150$ mm^{-1} and $g = 0.99$ for blood. Optical parameters for 1% intralipid were taken to be $\mu_a = 0$, $\mu_s = 2.0$ mm^{-1} and $g = 0.7$, as average values of those obtained from van Staveren *et al* (1991) and Flock *et al* (1992). Their values were 2.3 mm^{-1} and 1.7 mm^{-1} for μ_s and 0.61 and 0.78 for g respectively, with $\mu_a \approx 0$ for both groups.

2.2. Monte Carlo simulation of ODT

2.2.1. Modelling the Doppler process. Propagation of photons emitted from the probe into the medium and eventually backscattered and directed towards the detector was simulated by a *photon histories generator* as described in Smithies *et al* (1998).

Doppler shifts experienced at each scattering interaction with the moving medium in the vessel were included into the photon histories according to the expression

$$\Delta = (\boldsymbol{k}_o - \boldsymbol{k}_i) \cdot \boldsymbol{v} = \Delta \boldsymbol{k} \cdot \boldsymbol{v} \tag{5}$$

where $\boldsymbol{k}_i$ and $\boldsymbol{k}_o$ are the incoming and outgoing wavevectors for this particular interaction, and $\boldsymbol{v}$ is the velocity of the medium at the position of the interaction (see figure 1B). Successive Doppler shifts were accumulated for each photon as it propagated through the medium and experienced a total of n_j scattering interactions

$$\omega_d \equiv \omega_{Dj} = \sum_{k=1}^{n_j} \Delta_k. \tag{6}$$

This accumulated Doppler frequency was also stored in the histories file for backscattered photons along with their accumulated pathlength, the sequence of scattering positions and their angular and spatial coordinates for intersecting the detector surface (Smithies *et al* 1998).

2.2.2. Data processing and presentation. The data processing program was implemented with the AVS image analysis software (Advanced Visualization System, Waltham, MA) as a number of specially developed modules that integrate into the entire software package and utilizes standard AVS modules for data processing and graphics presentation (Upson *et al* 1989).

Results presented in this paper utilize several of the same modules that were developed for the simulation of OCT (Smithies *et al* 1998). These include the *data reader* and the *photon detector*, where the latter determines which of the read photons satisfy the user-specified detection criteria with respect to source coherence length (L_c), numerical aperture (NA), and confocality (δ) of the detector, the *photon counter* which registers the number of detected photons for each (x, z') scan position, and the *scattering events distribution*, which for a specified focus position displays a histogram of the number of photons detected as a function of number of scattering events.

Two modules are specific for the ODT simulation. The *average Doppler frequency* module generates a graph of average values of accumulated Doppler frequencies for photons detected at a series of specified (x, z') positions in a z'-scan. Each average is computed as

$$\bar{\omega}_D \equiv \bar{\omega}_{Di} = \frac{1}{n_i}\sum_{j=1}^{n_i}\omega_{Dj} \qquad i = 1, \ldots n_z \tag{7}$$

where n_i is the number of photons detected for position (x, z') and n_z is the number of z' positions probed. This module also generates the corresponding series of root mean square (rms) Doppler frequencies

$$\bar{\omega}_D^{\mathrm{rms}} \equiv \bar{\omega}_{Di}^{\mathrm{rms}} = \sqrt{\frac{1}{n_i}\sum_{j=1}^{n_i}\omega_{Dj}^2} \qquad i = 1, \ldots n_z. \tag{8}$$

The *Doppler frequency distribution* module displays for a specified position (x, z_i') a histogram of the accumulated Doppler frequencies ω_{Dj} (equation (6)) or the Doppler shifts Δ_{ijk} (equation (5)) from individual scattering interactions (k) for individual photons (j) for the total of n_i photons detected at focus position i.

3. Results

3.1. Experimental results

Figure 2 shows ODT images of the experimental phantom with blood flowing at an average velocity of 1.8 mm s^{-1} in the 280 μm diameter lumen of the tubing. The results are presented as a static intensity image (A) and a Doppler velocity image (B). The blood flow in the positive y-direction gives rise to positive Doppler frequencies within the lumen that have been converted to velocities as shown in panel B. Underneath the vessel there are spurious Doppler velocity noise signals. The appearance of signals in panel B implies that the backscattered intensity at those pixels has been removed from the static intensity image, and the lumen in panel A therefore appears black.

Concentrations of intralipid and blood were reduced by a factor of 2.8 in order to be equivalent to the Monte Carlo simulations in the number of scattering interactions for photons traversing the flow lumen. In some cases the blood suspension was further diluted to obtain stronger signals and thereby more reliable Doppler frequency information from underneath the vessel. Thus, imaging of 4% blood as in figure 2B would correspond to

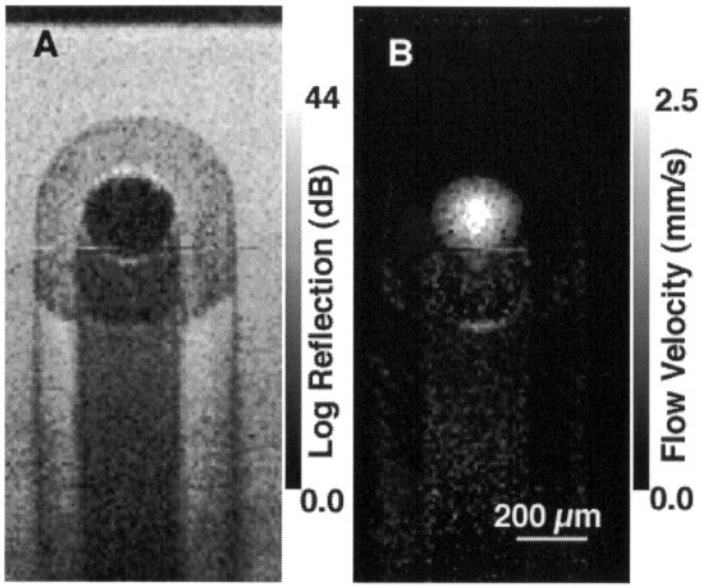

Figure 2. Experimentally recorded ODT images taken at 15° probe incidence angle showing the static backscattering intensity (A), and the Doppler velocity image (B). Glutaraldehyde-fixed canine RBCs at a volume fraction (haematocrit) of 4% suspended in 42% CsCl were flowing in a 280 μm inner diameter tube immersed in 2.8 × diluted 2% intralipid.

simulations with 4 × diluted blood in the 2.8 × smaller vessel specified for the Monte Carlo simulations. (4 × 2.8 dilution of undiluted blood at 45% nominal haematocrit, gives blood of 4% haematocrit.)

Figure 3A shows a velocity profile taken along the vertical diameter of the vessel imaged in figure 2, i.e. at 15° incidence. A corresponding profile recorded for 25° incidence of the probe is shown in figure 3B. Fitted parabolic functions demonstrate the agreement between experimental data and the theoretical velocity profile expected for laminar flow in a tube. Maximum velocity estimates for panels A and B were 2730 and 2620 μm s^{-1} respectively, with corresponding diameter estimates of 285 and 272 μm. The statistical precision of these estimates varied from 4 to 8% relative standard error of the mean. The isolated, strong signal about 150 μm underneath the vessel is an artefact, probably due to reflection (see figure 2). The Doppler velocity noise underneath the vessel seems to be similar in magnitude in figures 3A and 3B, and is predominantly positive due to the frequency estimation procedure (see discussion, section 4).

Figure 4 shows experimental frequency power spectra $G_f(0, \Delta z', f)$ obtained according to equation (1) from the raw data underlying figure 3 and representing regions above and below the vessel as well as at the centre of the lumen. Spectra representing backscattering from static intralipid are distributed around the carrier frequency (1600 Hz) with mean values in the range from 1560 to 1650 Hz, whereas spectra representing the centre of the lumen are shifted to higher frequencies, more so for the higher angle of incidence (figure 4B versus figure 4A). Standard deviations of the spectra above the vessel were 310 and 350 Hz for the incidence angles of 15° and 25° respectively (dotted curves), whereas corresponding values for spectra below the vessel were 610 and 650 Hz (thick full curves).

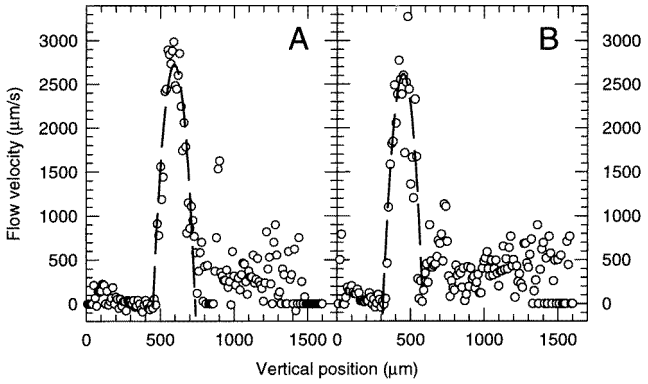

Figure 3. Experimental Doppler velocity profiles along a vertical line through the centre of the vessel lumen. The graph in panel A was obtained from data shown in figure 2B and represents a probe incidence angle of 15°. Panel B shows corresponding data for a 25° incidence angle. Open circles represent experimental frequency data converted to velocities according to equation (3). The broken curves show fitted parabolic curves having the maximum velocity, the vessel diameter and the vessel axis depth as free parameters to be estimated by the weighted nonlinear least squares fitting procedure.

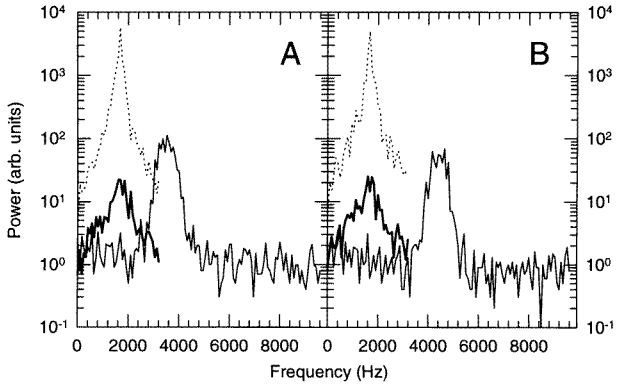

Figure 4. Experimental frequency power spectra $G_f(0, \Delta z', f)$ obtained according to equation (1) from the raw data underlying figure 3, i.e. representing incidence angles of 15° (A) and 25° (B). Spectra were averaged over intervals ($\Delta z'$) of 100 μm (10 pixels) above (dotted curves) and below (thick full curves) the vessel, and over 40 μm at the centre of the vessel (thin full curves).

3.2. Results from Monte Carlo simulations

Monte Carlo simulations were based on the geometry shown in figure 1 where the vessel wall was assumed to have zero thickness. In most of the following figures, as in figures 3 and 4, panel A will show results for the probe at 15° incidence angle and panel B results at 25°. The simulated geometry corresponds to an optical depth of 0.8 mfp (mean free path) units in intralipid ($g = 0.7$) at the top of the vessel, with an additional optical depth in blood ($g = 0.99$) increasing to 15 mfp units through the full diameter of the vessel. The deepest position, 100 μm underneath the vessel, corresponds to an optical depth of 1.2 in intralipid plus 15 in blood. To account for the non-vertical path, these values should be

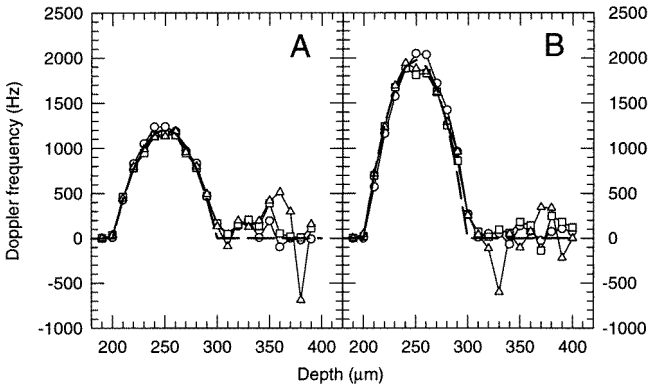

Figure 5. Doppler frequency profiles along the z-axis obtained from Monte Carlo simulations with the probe at incidence angles of 15° (A) and at 25° (B). Data are shown for source coherence length $L_c = 14$ μm and confocality angle $\delta = 0.5°$. Different symbols correspond to different numerical apertures of the detector: NA = 0.4 circles; NA = 0.2 squares; NA = 0.1 triangles. Values for the intralipid region above the vessel ($z' < 200$ μm) were systematically zero. The broken curve shows the frequency profile determined by the parabolic velocity profile specified as part of the input data for the simulation.

multiplied by the factors 1.02 and 1.05 for incidence angles of 10.9° and 18° in the medium, corresponding to the incidence angles of 15 and 25° respectively in air. The final optical pathlengths of detected photons are actually twice the above figures due to the round-trip path down to the focus depth and back to the detector.

Figure 5 shows average Doppler frequencies along a vertical scan through the centre of the vessel. The results demonstrate that the Doppler frequencies obtained from the Monte Carlo simulation approximate the mathematically expected frequencies quite well, and slightly better as the numerical aperture of the detector is decreased. Reducing the coherence length from 28 μm to 14 and 7 μm showed a similar but smaller effect in improving the accuracy of frequency estimates (results not shown). Reducing the confocality angle from 1° to 0.5 and 0.3° showed a comparable, minor improvement of the profiles, although variability due to low photon counts gave significant stochastic variability in the results for $\delta = 0.3°$ (results not shown). The frequency profiles show the expected increase in maximum value with increasing incidence angle of the probe (panel B versus panel A). In contrast, the random Doppler frequencies found for photons backscattered from the intralipid region underneath the vessel (310–400 μm depth) seem quite similar for the two different incidence angles.

Figure 6 shows the number of photons detected when using NA = 0.2, $L_c = 14$ μm and $\delta = 0.5°$ as detection parameters in the simulation. The number of photons detected with net positive and net negative Doppler frequencies are shown together with the total number of photons, which includes photons without a Doppler shift. Through the intralipid above the vessel, the total counts follow quite closely the mathematical expression of the extinction model for intralipid (Smithies *et al* 1998). As the probe focus position z' moves into the vessel, all detected photons carry positive Doppler frequencies. Towards the lower boundary of flow, the number of photons detected with a net negative Doppler frequency starts to increase. Underneath the vessel the numbers of positively and negatively Doppler shifted photons vary considerably due to low counts but appear nearly equal, although the number of positively shifted photons seems slightly higher than the number of negatively

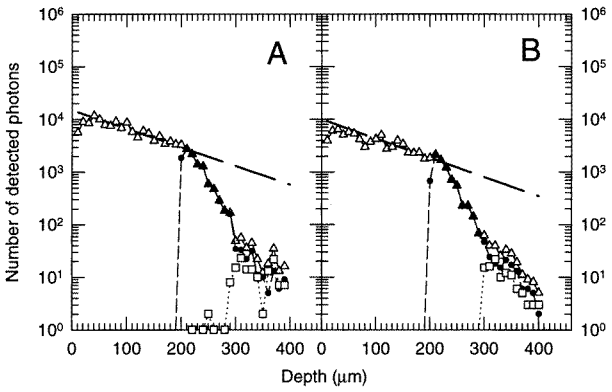

Figure 6. The number of detected photons as a function of depth in the simulated flow phantom, with the probe at incidence angles of 15° (A), and 25° (B), using the following detection parameters: NA = 0.2, $L_c = 14$ μm and $\delta = 0.5°$. Different symbols indicate photons detected with a net positive (full circles) or net negative (squares) Doppler frequency, as well as the total number of photons detected for each focus position (triangles), i.e. the sum of photons with positive, negative or zero Doppler frequency. The broken curve shows attenuation of photon counts according to the extinction model $\exp(-2\mu_s z'/\cos\alpha')$, using $\mu_s = 4$ mm s^{-1} for 2% intralipid.

shifted photons. The only difference between 15 and 25° incidence angles (figure 6A versus 6B) is the slightly higher numbers of detected photons for the lower incidence angle.

Photons backscattered from the flow axis have undergone an average of 15 ± 4 (SD) scattering events. Closer examination of the individual histories for photons backscattered from the central region of flow revealed that each photon experienced a series of stochastic Doppler shifts on the downward path through the vessel, a large, positive Doppler shift upon backscattering, and a series of stochastic Doppler shifts on the upward path through the vessel. Photons backscattered from underneath the vessel experienced the same stochastic shifts through the blood flow, but there was no Doppler shift from the backscattering event in the static intralipid. The result is therefore a random net Doppler frequency with an expected mean value of zero, but with actual positive and negative values varying stochastically between photons and from one focus position to the next.

Figure 7, which shows profiles of the rms Doppler frequencies according to equation (8), demonstrates more clearly the characteristic value of the random Doppler noise from regions underneath the vessel. The results suggest that the noise level is independent of the probe incidence angle, leading to a more favourable Doppler signal-to-noise ratio (i.e. flow-axis Doppler signal over Doppler noise signal from underneath the vessel) as the probe incidence angle is increased from 15° (figure 7A) to 25° (figure 7B).

Figure 8 shows spectra of Doppler shifts from individual interactions (open circles) as well as the accumulated Doppler frequencies for photons (full squares) detected with probe focus on the flow axis (upper panels) or below the vessel (lower panels). The results from the flow axis (figures 8A, B, open circles) showing bimodal distributions, demonstrate the clear distinction between the many small, random Doppler shifts from individual forward scattering events and the pronounced Doppler shifts due to backscattering. This distinction becomes even more pronounced as the probe incidence angle is increased from 15° (figure 8A) to 25° (figure 8B). The distributions of accumulated Doppler frequencies (full squares) approximate the distributions of backscattering Doppler shifts, but show less variability.

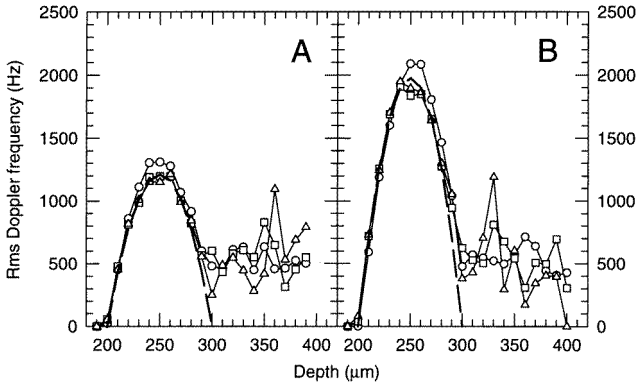

Figure 7. Profiles of the rms Doppler frequency (equation (8)) obtained from Monte Carlo simulation with the probe at 15° (A) and 25° (B) angles of incidence. Different symbols are as explained in the legend to figure 5.

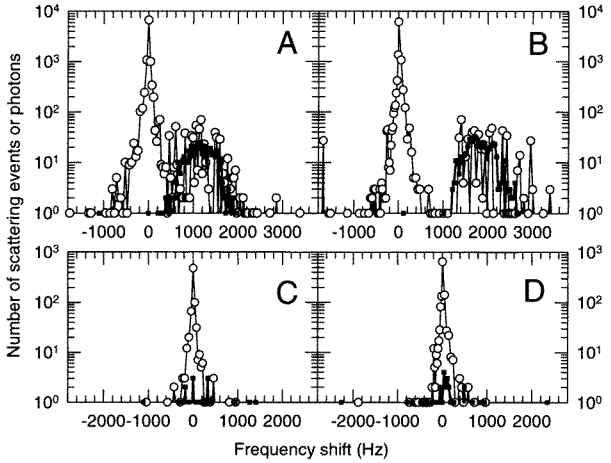

Figure 8. Distributions of Doppler shifts from individual interactions (open circles, thin curve) and accumulated Doppler frequencies for photons (full squares, full curve) detected with the probe focus on the flow axis at 250 μm depth (A, B) or aimed underneath the vessel at 340 μm depth (C, D). Results are shown for probe incidence angles of 15° (A, C) and 25° (B, D). Other detection parameters were: NA = 0.2, L_c = 14 μm and δ = 0.5°. Detected photons had an average of 18 and 20 scattering interactions for focus on the flow axis and incidence angles of 15° and 25° respectively. For focus at 340 μm depth, these numbers were 34 and 36 respectively.

The data from underneath the vessel (figures 8C, D) show similar distributions for the two different incidence angles. Both Doppler shifts for individual interactions (open circles) and accumulated Doppler frequencies for detected photons (full squares) are distributed around zero, with similar widths for both incidence angles of the probe. Spectra of individual Doppler shifts from focus positions 310, 340 and 370 μm depth had standard deviations ranging from 65 to 100 Hz with no systematic difference between incidence angles of 15° and 25°. Standard deviations for corresponding spectra of accumulated Doppler frequencies were in the range of 300 to 680 Hz (results not shown). According to the analysis in

appendix (see equation (A4)), standard deviations of individual Doppler shifts, σ_Δ, and those of accumulated Doppler frequencies, σ_D, are related by the number of scattering interactions with the flowing medium, $\bar{m}_j$, in the following way:

$$\sigma_D = \sqrt{\bar{m}_j}\sigma_\Delta. \tag{9}$$

Estimates of $\bar{m}_j$ obtained by inserting pairs of values σ_Δ and σ_D from the three different depths mentioned above were 29, 36 and 22 for 15° incidence angle, and 48, 46 and 31 for 25° incidence angle. Corresponding theoretical values (see equation (A5)) are 30 and 32 scattering events respectively.

Figure 9 shows a more systematic investigation of the standard deviation of Doppler frequency distributions such as those shown in figure 8 (full squares). Results are shown for the various probe focus positions through the vessel and through the intralipid underneath. Within the vessel, standard deviations are significantly smaller for smaller numerical apertures, show a maximum around the centre of the vessel, and diminish away from the flow axis, suggesting a value proportional to the parabolic velocity profile within the vessel (figure 9A). This finding was supported by results from a simulation based on constant velocity throughout the lumen (flat velocity profile), in which standard deviations were nearly constant through the diameter of the vessel (results not shown). Underneath the vessel the standard deviations in figure 9 essentially correspond to the rms noise levels seen in figure 7 (rms values approximate the SD values for stochastic variables which have zero mean values; see also equation (A10)).

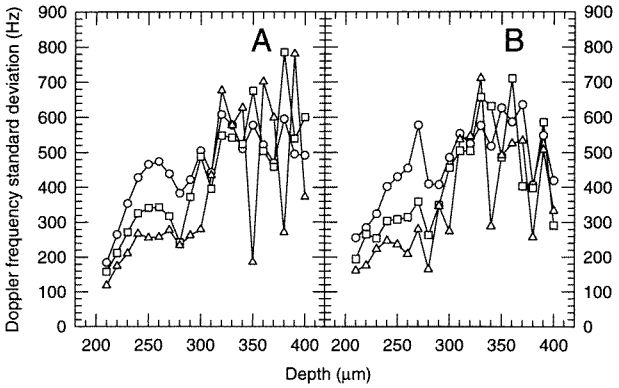

Figure 9. Standard deviations of simulated Doppler frequency spectra obtained for probe incidence angles of 15° (A) and 25° (B). Results are shown for different numerical apertures of the detector: NA = 0.4 circles, NA = 0.2 squares, NA = 0.1 triangles, with $L_c = 28$ μm and $\delta = 0.5°$ in all cases. Use of $L_c = 14$ μm gave similar results, although greater variability due to fewer detected photons.

Table 1 lists standard deviations of Doppler frequencies on the flow axis at 250 μm depth, as well as mean values over four focus positions underneath the vessel (310, 340, 370 and 400 μm). Values from the flow axis seem to be independent of incidence angle (upper part of table 1), but vary with numerical aperture of the detector with values about 300 Hz for NA = 0.2 and 430 Hz for NA = 0.4. Even for a 2 × dilution of the blood and when a flat velocity profile is assumed throughout the vessel lumen (lower part of table 1), the standard deviations of the on-axis Doppler frequency remain comparable for a given NA. Only for an increased on-axis velocity (3 mm s^{-1} instead of 2 mm s^{-1}) does the standard deviation of the Doppler frequency increase significantly, and it varies in this

Table 1. Mean standard deviations (± standard error of the mean) of Doppler frequencies determined on the flow axis at 250 μm depth and from a region underneath the vessel, represented by averaging values from depth positions 310, 340, 370 and 400 μm. All data represent the confocality angle $\delta = 0.5^\circ$, but results for source coherence lengths of both 14 and 28 μm were included in the averages. Standard flow conditions represent a parabolic velocity profile having maximum velocity of 2 mm s^{-1} on the axis, corresponding to a diameter-average velocity of 1.33 mm s^{-1}.

Cases	Nominal on-axis doppler frequency (Hz)	SD (Hz) of Doppler frequency on flow axis		SD (Hz) of Doppler noise at 310–400 μm depth	
		NA = 0.2	NA = 0.4	NA = 0.2	NA = 0.4
Standard flow at various incidence angles					
10°	813.3	312.6 ± 6.0	453.5 ± 1.4	500.3 ± 51.2	466.4 ± 5.9
15°	1212	331.3 ± 9.3	447.4 ± 18.5	492.4 ± 68.8	466.2 ± 4.7
20°	1602	286.4 ± 2.6	409.6 ± 10.2	520.3 ± 16.0	515.6 ± 3.8
25°	1979	307.0 ± 0.6	418.2 ± 11.5	481.3 ± 49.3	530.6 ± 33.0
30°	2342	263.2 ± 6.8	412.9 ± 25.5	443.1 ± 34.7	605.6 ± 18.5
Different flows at 15° incidence angles					
2 × dilute blood	1212	320.0 ± 7.1	477.6 ± 11.3	272.6 ± 45.1	270.8 ± 13.5
Flat velocity profile	1212	311.7 ± 6.0	479.3 ± 4.0	873.4 ± 81.1	744.6 ± 11.5
3 mm s^{-1} on-axis velocity	1818	503.3 ± 15.5	710.2 ± 0.1	714.9 ± 16.9	725.1 ± 19.4

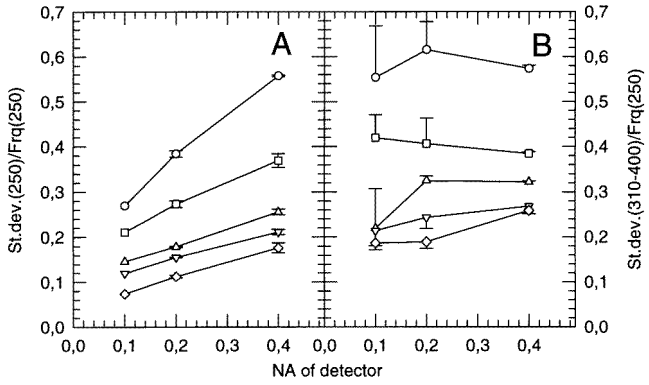

Figure 10. Panel A: Precision of Doppler frequencies determined for the position of maximum velocity on the flow axis at 250 μm depth, i.e. standard deviations of Doppler frequency spectra divided by the nominal Doppler frequency at the flow axis. Data are shown as a function of NA of the detector for various angles of incidence of the probe (○, 10°; □, 15°; △, 20°; ▽, 25°; ◇, 30°). Panel B: Relative Doppler noise signal detected from underneath the vessel, i.e. Doppler noise averaged for focus positions 310, 340, 370 and 400 μm depth and expressed relative to the nominal Doppler frequency at the flow axis. Error bars in both panels indicate one standard error of mean values obtained by averaging over data for two different source coherence lengths (14 and 28 μm) and from four different focus positions (panel B only). Error bars are shown only to one side in order to improve clarity.

case proportionally with the velocity. The results indicate that the precision, i.e. relative standard deviation of the Doppler frequency on the flow axis will be best for large incidence angles and low numerical aperture, as illustrated in figure 10A. This figure also contains

results for NA = 0.1, which further support the finding of increasing standard deviation of Doppler frequencies with increasing numerical aperture.

The values for Doppler noise underneath the vessel shown in the last two columns of table 1, show no systematic changes with incidence angle or numerical aperture of the detector probe. These results are further analysed in figure 10B, where standard deviations are expressed relative to the nominal Doppler frequencies on the flow axis. The figure also includes values for NA = 0.1, which have rather large standard errors due to the small numbers of detected photons. However, the data for NA = 0.1 are not significantly different from values for the higher numerical apertures.

Figure 11 shows results based on the theoretical analysis in the appendix. According to equation (A6), the theoretical value for the standard deviation of spectra of accumulated Doppler noise for a particular focus position, is, expressed in Hz

$$\sigma_D = \frac{\bar{v}}{\lambda}\sqrt{2(1-g)\mu_s T \cos\alpha'} \tag{10}$$

where $\bar{v}$ denotes the average flow velocity along the photon path. Theoretical values according to equation (10) were calculated for the various flow conditions represented in table 1 and plotted to show the correlation with corresponding Monte Carlo results. The fitted regression line in figure 11 indicates a proportionality relationship. Although the data show reasonably good correlation, the proportionality constant (0.60) is significantly different from the value of 1.0 which would be expected if equation (10) were a correct expression for the standard deviations of Doppler noise spectra for detected photons.

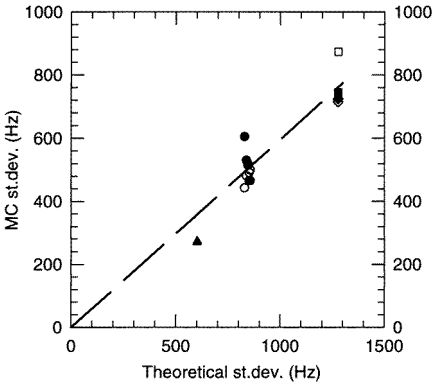

Figure 11. Correlation between theoretical values for standard deviations of Doppler noise from underneath the vessel according to equation (10) and corresponding results from Monte Carlo simulations. The MC data are from table 1 (last two columns), with open symbols for NA = 0.2 and full symbols for NA = 0.4. Circles indicate standard flow conditions (parabolic velocity profile with $v_o = 2$ mm s^{-1}, $\bar{v} = 1.33$ mm s^{-1}) at 10 to 30° angles of incidence; triangles indicate standard flow of 2 × diluted blood at 15° incidence angle; diamonds indicate 50% increased velocity under otherwise standard conditions ($v_o = 3$ mm s^{-1}, $\bar{v} = 2$ mm s^{-1}); and squares represent a flat velocity profile ($v_o = 2$ mm s^{-1}, $\bar{v} = 2$ mm s^{-1}) using a 15° incidence angle. The broken line through the origin is fitted to illustrate a proportionality relationship ($y = 0.60x$).

Figure 12 shows simulation results that address the positional precision of Doppler velocity determinations. For this purpose a constant velocity was defined throughout the lumen of the vessel. The results show average Doppler frequencies for a series of focus positions going vertically into the vessel from above (figure 12A) and out of the vessel

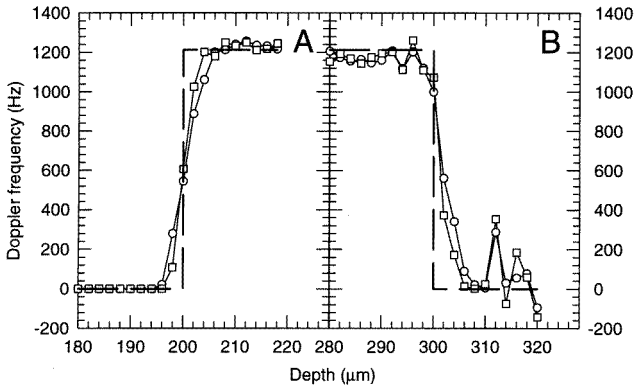

Figure 12. Diagrams showing the ability to locate a step function in velocity as determined by Doppler frequency profiles from simulated scans vertically into the top (A) and through the lower boundary (B) of the vessel which was modelled with a flat velocity profile. Data are shown for source coherence lengths of 28 μm (circles) and 14 μm (squares). Other detection parameters were probe incidence angle of 15°, NA = 0.2, $\delta = 0.5°$. The broken curve shows the step function in Doppler frequency determined by the velocity profile specified for the simulation.

at the lower boundary (figure 12B). Values are shown for source coherence lengths of 28 and 14 μm, and indicate slightly steeper transition curves for the shorter coherence lengths. The data, which represent NA = 0.2, give a slightly steeper transition than obtained for NA = 0.4 (results not shown). The results demonstrate that a step function in velocity can be localized with an accuracy of about 6 μm (interval for increase from 20% to 80% of step) at the top of the vessel and about 8 μm at the bottom boundary of the vessel, with a slight systematic shift (2 μm) of the midpoint depth to 302 μm instead of 300 μm for the latter determination.

4. Discussion

In our work with experimental optical Doppler tomography (ODT) we regularly observe random Doppler noise shadowing underneath regions of detected flow. This shadowing, thought to be an effect caused by multiple scattering of light passing through the overlying flow region, as well as the question of accuracy of estimated flow velocities in ODT imaging, motivated the formulation of a Monte Carlo model for simulating the ODT measurement process.

The model was based on Monte Carlo simulation of light propagation and scattering in turbid media, as used in other fields of bio-optics, such as studies of laser Doppler flowmetry (de Mul 1992, de Mul *et al* 1995, Jentink *et al* 1990, Koelnik *et al* 1994). Monte Carlo simulation of photon propagation in the scattering medium was combined with geometrical optics modelling of the OCT/ODT probe, including implementation of the antenna theorem (Siegman 1966, Schmitt *et al* 1994) which takes into account the confocal-like detection of the heterodyne interferometric ODT measurement procedure.

In a companion publication (Smithies *et al* 1998) we have described how instrumentation parameters such as the source coherence length, and the numerical aperture and confocality angle of the detector influence the signal detected in OCT of static media. In the present report most results were obtained using detection parameters that closely represent the laboratory instrumentation (i.e. source coherence length, $L_c = 14$ μm; numerical aperture

of detector, NA = 0.2). A confocality angle of $\delta = 0.5^\circ$ was used for most investigations, even if the physical probe of the instrument represents a value of $\delta = 0.06^\circ$, since a decrease in the number of detected photons will occur with increasing confocality of the detector. Monte Carlo simulation of OCT imaging in blood demonstrated good localization of the signal to the nominal focus position of the probe down to an optical depth exceeding 35 scattering mean free path units (1 mfp $= 1/\mu_s$) (Smithies *et al* 1998).

Based on the above-mentioned findings it was not unexpected that estimation of Doppler frequencies from the region of blood flow showed good localization to the actual position of the vessel (figure 5). A significant finding in the present work is that the average Doppler frequency for photons detected from a particular focus position was determined with an accuracy of only 3 to 4% deviation from the mathematically expected Doppler frequency (region of maximum flow, depth positions 230–270, figure 5). This is remarkable, considering that the spectra of observed Doppler frequencies were quite broad, with standard deviations typically exceeding 250 Hz (table 1, figure 9), compared with the nominal Doppler frequencies of 1212 and 1979 Hz on the flow axis in figures 5A and 5B respectively. Evidently, the averaging of Doppler frequencies over many photons for each focus position represents such a robust estimation procedure that the resulting mean value quite accurately approximates the true frequency.

The Doppler frequency noise detected from underneath the vessel (figure 5) is due to the series of random Doppler shifts experienced as the photon passes through the blood flow region before and after the backscattering event in intralipid underneath the vessel. The resulting accumulated Doppler frequency for each detected photon is expected to be zero, due to approximately equal numbers of photons with randomly positive and negative Doppler frequencies detected from underneath the flow region (figure 6). Photons carrying a positive Doppler frequency seem, however, to barely but systematically outnumber negatively shifted photons (figure 6, 300–400 μm depth). Correspondingly, the Doppler noise more frequently seems to assume a positive rather than negative value (figure 5, 300–400 μm depth). These effects are small, but may be due to the oblique incidence of the probe which introduces an asymmetry and causes the mean backscatter position to shift to slightly positive y-values for large probing depths in intralipid (Smithies *et al* 1998).

Another significant finding in the present investigation is that the Doppler noise level underneath the vessel (figure 7) is essentially independent of the incidence angle of the probe, even if a larger incidence angle corresponds to higher average Doppler frequencies detected from the flow region. The standard deviations of Doppler noise spectra from underneath the flow region are generally greater than the standard deviations of Doppler frequencies detected from the region of blood flow (figure 9). This may seem surprising since the variance of the detected Doppler frequency may be expressed as a sum (over scattering locations) of contributions from individual scattering events along the paths of individual photons (equation (A4)). Furthermore, the difference between photons backscattered from flowing blood and those backscattered from the static intralipid underneath the blood vessel is essentially that the latter carry no contribution to the Doppler frequency variance from the backscattering event (since the Doppler shift is zero). The reason for the smaller standard deviations of Doppler spectra from blood than from the intralipid region underneath the vessel must therefore be that the incoming and outgoing photon paths are more closely correlated for backscattering from blood, leading to Doppler shifts from individual scattering events that more exactly cancel each other and generate less variance. Scattering in intralipid is more isotropic ($g = 0.7$) and backscattering from underneath the vessel will conceivably give rise to photon paths that differ more between the incoming and outgoing paths, leading to Doppler shifts demonstrating greater variance.

Similar arguments can serve to explain the finding that the standard deviation of average Doppler frequencies from within the vessel seems to follow quite closely the parabolic frequency profile determined by the parabolic velocity profile (most evident in figure 9A).

Our finding that the standard deviations of average Doppler frequencies measured within the vessel increase with increasing numerical aperture of the detector (figures 9 and 10A) can be explained by simple consideration of the variability in Doppler frequency shifts represented by backscattering events involving marginal rays at minimum and maximum angles with the flow axis, i.e. $(90^\circ - \alpha - \theta)$ and $(90^\circ - \alpha + \theta)$ respectively, giving rise to maximal and minimal Doppler frequencies.

The results in figure 10A indicate that especially for small incidence angles (10 to 15°), the precision of the estimated average Doppler frequency will be considerably improved by using a low-NA detector. This improvement, however, comes only at the cost of reduced signal strength.

Figures 10B and 11 summarize our findings concerning Doppler noise detected from underneath the vessel. To reduce Doppler noise in the shadow region underneath the region of blood flow, relative to the strength of the Doppler signal from the flow region, the obvious strategy is to use a relatively large incidence angle (figure 10B). In practice, however, this approach will be limited by loss of backscatter intensity and possible artefacts in the image that may be registered due to the oblique passage of light through structures lying outside the imaged plane.

Although the results in figure 11 represent reasonably good proportionality between theoretical and Monte Carlo results for the standard deviations of Doppler noise spectra, observed values are only 60% of theoretical values calculated according to equation (10). The assumption underlying equation (A6) that the individual Doppler shifts Δ_k which contribute to the accumulated Doppler frequency ω_D, are independent, may not be fulfilled. However, values for $\bar{m}_j$ obtained by inserting observed values for σ_Δ and σ_D into equation (9) which is based on the assumption of independent Doppler shifts, agree quite well with the number of scattering events expected from the optical thickness of the flow region, thus supporting the underlying assumption of independence.

Another explanation for systematically smaller observed standard deviations than predicted by equation (10), may be that ODT selectively detects photons that are extremely forward-scattered (apart from the backscattering event). Such selective detection of minimally scattered photons was indeed observed in our simulation of OCT (Smithies *et al* 1998). If we define an effective anisotropy parameter $g_{\text{eff}} = \overline{\cos\varphi}$ for detected photons, a value of $g_{\text{eff}} = 0.996$ (as opposed to $g = 0.99$) inserted into equation (10) would yield theoretical standard deviations equal to those observed in the Monte Carlo experiments. The fact that values for the $2\times$ diluted blood (full triangles, figure 11) fall below the regression line might indicate that for lower optical thickness ($\mu_s T$), forward-scattered photons are even more selectively detected and characterized by an even higher value for g_{eff}.

It is interesting to observe that the correlation between simulated and theoretical values in figure 11 is better for NA = 0.2 (open circles) than for NA = 0.4 (full circles). In fact, for the analysis in the appendix leading to equation (10), the numerical aperture of the probe was assumed to be vanishingly small, corresponding to photon paths close to the optical axis of the probe, at incidence angle α. The results in figure 11 (full versus open circles) suggest that there may be an effect of numerical aperture for large incidence angles, which is not contained in equation (10).

The investigation of how closely a step function in flow velocity may be localized by ODT, shown in figure 12, is in good agreement with our previous studies of

signal localization in static media (Smithies *et al* 1998), where we found that actual backscatter position falls short of the nominal depth by about 2% at an optical depth of 15 in blood. This would cause a shift of 2 μm in the detected position of the lower boundary of the vessel (i.e. 2% of the blood vessel diameter), as observed in figure 12B.

The Monte Carlo simulation results are supported by our experimental investigations, although direct comparison may in some cases require insight into details of the data processing algorithms. Thus, the Doppler noise detected from underneath the vessel is mostly positive in experimental Doppler profiles (figure 3), whereas the simulated profiles (figure 5) show more comparable occurrence of positive and negative Doppler noise signals. The dominance of positive noise in the experimental data is due to the data processing algorithm used to estimate the centroid of the fringe intensity power spectra (see equation (4)). This estimation is taken over an interval from 0 to 9600 Hz (see figure 4). The carrier frequency is at 1600 Hz. Contributions from white noise in the 8000 Hz frequency interval above the carrier frequency will therefore tend to outweigh contributions from the 1600 Hz interval below the carrier frequency, resulting in a net positive Doppler noise frequency in figure 3. For the estimation of means and standard deviations of noise spectra above and below the vessel in figure 4, an interval from 0 to 3200 Hz was used, i.e. a symmetric interval around the carrier frequency of 1600 Hz, in order not to introduce overweighting of high-frequency noise contributions.

Standard deviations of experimental Doppler frequency noise spectra from underneath the vessel were greater than those of corresponding spectra from above the vessel (figure 4). Although several sources of noise contribute to the width of experimental Doppler spectra, the increased standard deviations of spectra from underneath the vessel are taken to indicate Doppler broadening caused by the blood flow. In agreement with Monte Carlo results, standard deviations of experimental Doppler noise spectra revealed no significant differences between values representing different probe incidence angles, despite the higher Doppler frequencies from the flow region for the larger incidence angles.

Although several important aspects of OCT/ODT were not included in the present model, for example spatial correlation properties of the medium, and even if simulation of the full confocality of the physical detector ($\delta = 0.06^\circ$) was not feasible due to computer run-time limitations, our preliminary results demonstrate the usefulness of Monte Carlo modelling for increasing the understanding of OCT/ODT.

Acknowledgments

This work was performed while T Lindmo was a visiting scientist at the Beckman Laser Institute, on sabbatical leave from the Norwegian University of Science and Technology and supported by the Research Council of Norway. The authors wish to thank M van Gemert, J de Boer, S Srinivas and D Dave for helpful discussions. This project is supported by research grants awarded from the Institute of Arthritis and Musculoskeletal and Skin Diseases (1R01-AR43419) at the National Institutes of Health, and the Whitaker Foundation (21025 and 23281). Institute support from the Office of Naval Research (N00014-94-1-0874), Department of Energy (DE-FG03-91ER61227), the National Institutes of Health (Laser Microbeam and Medical Program, RR-01192), and the Beckman Laser Institute Endowment is also gratefully acknowledged.

Appendix

With reference to the geometry shown in figure 1B, the Doppler shift resulting from interaction k for photon j when the probe is aimed at focus position i is

$$\Delta_{ijk} \equiv \Delta_k = (\boldsymbol{k}_o - \boldsymbol{k}_i) \cdot \boldsymbol{v} = 2kv \cos\alpha' \sin\frac{\varphi}{2} \cos\zeta \qquad k = 1, 2, \ldots m_j \tag{A1}$$

where $\boldsymbol{v}$ is the velocity at the scattering position under consideration and m_j is the number of scattering interactions in the flowing medium for photon j (as opposed to the total number of scattering events for photon j, n_j). The expected value, i.e. mean value, of Δ_k is $E[\Delta_k] = 0$ since the scattering angle φ takes on positive and negative values with equal probability and the azimuthal angle ζ varies uniformly between 0 and 2π. The variance of Δ_k is

$$\mathrm{Var}(\Delta_k) \equiv \sigma_\Delta^2 \equiv E[(\Delta_k - E[\Delta_k])^2] = E[\Delta_k^2] = (2kv\cos\alpha')^2 E\left[\left(\sin\frac{\varphi}{2}\cos\zeta\right)^2\right].$$

The scattering angle is independent of the azimuthal angle, and the expectation values are therefore obtained as

$$E\left[\left(\sin\frac{\varphi}{2}\cos\zeta\right)^2\right] = E\left[\left(\sin\frac{\varphi}{2}\right)^2\right] E[(\cos\zeta)^2] = E\left(\frac{1-\cos\varphi}{2}\right)\cdot\frac{1}{2}$$
$$= \frac{1-\overline{\cos\varphi}}{2}\cdot\frac{1}{2} = \frac{1-g}{4}$$

Thus

$$\sigma_\Delta = kv\cos\alpha'\sqrt{(1-g)}. \tag{A2}$$

The accumulated Doppler frequency for photon j detected from focus position i is

$$\omega_D \equiv \omega_{Dj} = \sum_{k=1}^{m_j} \Delta_k \qquad j = 1, 2, \ldots n_i. \tag{A3}$$

From elementary theory of statistics, the mean and variance of a sum of independent random variables are known to be the sum of mean values and sum of variances respectively. For equation (A3), this means $E[\omega_D] = 0$ and

$$\mathrm{Var}(\omega_D) \equiv \sigma_D^2 = \sum_{k=1}^{m_j} \mathrm{Var}(\Delta_k) = m_j \mathrm{Var}(\Delta_k) = m_j\sigma_\Delta^2. \tag{A4}$$

The number of scattering interactions in the flowing medium is

$$m_j \equiv \int_S \mu_S \,\mathrm{d}s = \frac{2\mu_S T}{\cos\alpha'} \tag{A5}$$

where the integral is taken along the photon path, S, and the last expression is given for a (round-trip) traverse at an incidence angle of α (α' in the medium) through a flowing medium of vertical thickness T. By combining equations (A2), (A4) and (A5), we obtain

$$\sigma_D = k\bar{v}\sqrt{2(1-g)\mu_S T\cos\alpha'} \tag{A6}$$

where $\bar{v}$ denotes the average flow velocity at the scattering locations along the photon path.

The average Doppler frequency for detected photons from focus position i is

$$\bar{\omega}_D \equiv \bar{\omega}_{Di} = \frac{1}{n_i}\sum_{j=1}^{n_i} \omega_{Dj} \qquad i = 1, 2, \ldots n_z \tag{A7}$$

with $E[\bar{\omega}_D] = 0$, and

$$\mathrm{Var}(\bar{\omega}_D) \equiv \sigma_D^2 = \frac{1}{n_i}\mathrm{Var}(\omega_D) = \frac{\bar{m}_j}{n_i}\sigma_\Delta^2 \tag{A8}$$

where $\bar{m}_j$ denotes the average number of scattering interactions in the flowing medium for photons detected from focus position i. We note that $\mathrm{Var}(\bar{\omega}_D)$ decreases as the number of detected photons, n_i, is increased.

For the rms value

$$\bar{\omega}_D^{\mathrm{rms}} \equiv \bar{\omega}_{Di}^{\mathrm{rms}} = \sqrt{\frac{1}{n_i}\sum_{j=1}^{n_i}\omega_{Dj}^2}$$

$$E[(\bar{\omega}_D^{\mathrm{rms}})^2] = \frac{1}{n_i}\sum_{j=1}^{n_i}E[\omega_{Dj}^2] = \frac{n_i}{n_i}E\left[\left(\sum_{k=1}^{\bar{m}_j}\Delta_k\right)^2\right] = E\left[\sum_{k=1}^{\bar{m}_j}\Delta_k^2\right]. \tag{A9}$$

In the squaring of the sum in the expression above, the cross-terms $\Delta_p\Delta_q$ vanish for $p \neq q$ due to the expectation operator. Thus

$$E[(\bar{\omega}_D^{\mathrm{rms}})^2] = \bar{m}_j E[\Delta_k^2] = \bar{m}_j\sigma_\Delta^2 = \sigma_D^2.$$

Hence

$$E[\bar{\omega}_D^{\mathrm{rms}}] = \sqrt{\bar{m}_j}\sigma_\Delta = \sigma_D. \tag{A10}$$

References

Chen Z, Milner T E, Dave D and Nelson J S 1997a Optical Doppler tomographic imaging of fluid flow velocity in highly scattering media *Opt. Lett.* **22** 64–6

Chen Z, Milner T E, Srinivas S, Lindmo T, Dave D and Nelson J S 1997b Optical Doppler tomography for noninvasive imaging of *in vivo* blood flow *Proc. SPIE* **2981** 112–18

Chen Z, Milner T E, Srinivas S, Wang X J, Malekafzali A, Van Gemert M J C and Nelson J S 1997c Noninvasive imaging of *in vivo* blood flow velocity using optical Doppler tomography *Opt. Lett.* **22** 1119–21

de Mul F F M 1992 Monte Carlo simulations of laser Doppler blood-flow measurements in tissue: reply to comment *Appl. Opt.* **31** 440

de Mul F F M, Koelnik M H, Kok M L, Harmsma P J, Greve J and Graaff R 1995 Laser Doppler velocimetry and Monte Carlo simulations on models for blood perfusion in tissue *Appl. Opt.* **34** 6595–611

Flock S T, Jacques S L, Wilson B C, Star W M and van Gemert M J C 1992 Optical properties of Intralipid: a phantom medium for light propagation studies *Lasers Surg. Medicine* **12** 510–19

Hawkey C M and Dennett T B 1989 *Color Atlas of Comparative Veterinary Hematology* (Ames: Iowa State University Press) p 17

Jacques S L 1996 Tissue optics *SPIE Short Course Note* SC34 26

Jentink H W, de Mul F F M, Hermsen R G A M, Graaff R and Greve J 1990 Monte Carlo simulations of laser Doppler blood flow measurements in tissue *Appl. Opt.* **29** 2371–81

Koelnik M H, de Mul F F M, Greve J, Graaff R, Dassel A C M and Aarnoudse J G 1994 Laser Doppler blood flowmetry using two wavelengths: Monte Carlo simulations and measurements *Appl. Opt.* **33** 3549–58

Schmitt J M, Knüttel A and Yadlowsky M 1994 Interferometric versus confocal techniques for imaging microstructures in turbid biological media *Proc. SPIE* **2135** 251–62

Siegman A E 1966 The antenna properties of optical heterodyne receivers *Appl. Opt.* **5** 1588–94

Smithies D J, Lindmo T, Chen Z, Nelson J S and Milner T E 1998 Signal attenuation and localization in optical coherence tomography studied by Monte Carlo simulation *Phys. Med. Biol.* **43** 3025–44

Stern M D 1993 Two-fiber laser Doppler velocimetry in blood: Monte Carlo simulation in three dimensions *Appl. Opt.* **32** 468–76

Upson C, Faulhaber T, Kamis D, Schlegel D, Vroom J, Gurwitz R and Dam A 1989 The application visualization system: a computational environment for scientific visualization *IEEE Comp. Graphics Appl.* **9** 30–42

van Staveren H J, Moes C J M, van Marle J, Prahl S A and van Gemert M J C 1991 Light scattering in Intralipid-10% in the wavelength range 400–1000 nm *Appl. Opt.* **30** 4507–14

Wang X, Milner T E, Chen Z and Nelson J S 1997 Measurement of fluid-flow-velocity profile in turbid media by the use of optical Doppler tomography *Appl. Opt.* **36** 144–9

Wang X J, Milner T E and Nelson J S 1995a Characterization of fluid flow velocity by optical Doppler tomography *Opt. Lett.* **20** 1337–9

——1995b Application of optical coherence interferometry to measure the spatial profile of fluid flow velocity *Proc. SPIE* **2546** 341–6

Weast R C, Astle M J and Beyer W H 1984 *CRC Handbook of Chemistry and Physics* 65th edn (Boca Raton, FL: CRC) p D–229

Yaroslavsky A N, Yaroslavsky I V, Goldbach T and Schwarzmaier H J 1996 The optical properties of blood in the near infrared spectral range *Proc. SPIE* **2678** 314–24